Current Ripple Analysis of Three-Phase Vienna Rectifier Considering Inductance Variation of Powder Core Inductor

Tao Wang, Changsong Chen, Tianchang Liu, Zeyun Chao, and Shanxu Duan, *Senior Member, IEEE*

***Abstract*—Three-phase three-level Vienna rectifier using powder core inductors has been widely used for power conversion. Inductor current ripple analysis of rectifier is essential for pulsewidth modulation method optimization, loss estimation, filter inductor design, etc. However, it is hard to analyze the current ripple of Vienna rectifier. Moreover, the inductance of powder core inductor varies with sinusoidal input current, which makes it even more complicated. In this article, a current ripple analysis method for three-phase Vienna rectifier considering the inductance variation of the powder core inductor is presented. The current ripple distribution of Vienna rectifier with constant inductance is studied based on the space vector approach. To determine the current ripple of Vienna rectifier with powder core inductors, an inductor voltage calculation method considering inductance variation is proposed. The compensation voltage is introduced to compensate for the effect of inductance variation on current ripple. Then, the analytical expression of the peak-to-peak current ripple with powder core inductor is derived. In addition, a design method of powder core inductor is proposed based on the analytical expression. At last, the correctness of the analytical result is verified by both simulation and experiment.**

***Index Terms*—Current ripple analysis, inductor design, powder core inductor, three-phase three-level rectifier, Vienna rectifier.**

I. Introduction

THREE-PHASE three-level Vienna rectifier has been widely used in power conversion owing to the advantages of high efficiency, high power density, simple structure, and high reliability [1], [2]. The filter inductors are essential for power converters and have influence on the efficiency and power density of converters. The commonly used magnetic materials of filter inductors in power converters include the ferrite and powder cores [3]–[5]. Compared with the ferrite, the powder cores have the advantages of high saturation flux density, no fringing losses, and soft saturation. Therefore, the losses and size of the filter inductor can be reduced using powder core. The powder cores have been widely used as the magnetic material of filter inductors for power converters [6]–[12]. In [6], the powder cores are applied in a 5-kW single-phase bidirectional inverter. The inductance variation is from 650 μH to 4.6 mH and the efficiency of the system reaches 97.5%. In [7], the powder cores are used in a 20-kHz, 10-kVA three-phase bidirectional inverter. In [11], the powder E-cores from magnetics are used as the filter inductors of a 10-kW three-phase, three-level pulsewidth modulation (PWM) rectifier. The switching frequency is 48 kHz and a filter power density of 13.1 kW/dm3 is achieved. In [12], the powder cores from Micrometals are used as the filter inductors of a 10-kW three-phase Vienna rectifier and the power density of the system is 14.1 kW/dm3. As mentioned above, the powder core inductors have been used in three-phase inverter, three-phase two-level (2L) rectifier, three-phase three-level rectifier, Vienna rectifier, etc. However, the inductance of the powder core varies with the inductor current due to the soft saturation, which has impacts on the performance of power converters.

The modulation methods have impacts on the current ripple of the rectifier. Several modulation methods such as carrier-based PWM) [13], [14], space vector modulation [15], [16] and discontinuous PWM [17]–[20] have been developed for three-phase Vienna rectifier. However, these papers have not shown a detailed analysis of current ripple.

The research of the current ripple plays an important role in filter inductor design, loss estimation, and modulation method optimization. The value of filter inductor is designed based on the maximum value of current ripple and the maximum current ripple of filter inductor is typically limited to 20%–40% of the nominal peak current [21]–[24]. In addition, the core loss of the filter inductor is based on the peak-to-peak flux density (ΔB) [25]–[27], which is derived by current ripple. Moreover, several modulation optimization methods have been proposed based on the current ripple analysis. In [28], a three-carrier-based SPWM scheme is presented to reduce the current ripple of the line and neutral current. In [29] and [30], a new switching sequence called hybrid PWM technique is developed for three-phase 2L inverter and the RMS value of current ripple is reduced. In [31], the current ripple characteristic of zero common-mode voltage PWM sequence is analyzed and a simple algorithm is developed to reduce the RMS value of current ripple. In [32], a variable switching frequency scheme is proposed to minimize switching loss of a single-phase inverter. In [33], a new variable frequency

Manuscript received January 8, 2019; revised May 18, 2019 and September 2, 2019; accepted September 22, 2019. Date of publication September 30, 2019; date of current version February 11, 2020. This work was supported by the National Key Research and Development Program of China (Key technologies of high performance charger for electric vehicles based on advanced power semiconductors, no. 2018YFB0106300). Recommended for publication by Associate Editor F. Luo. *(Corresponding author: Changsong Chen.)*

The authors are with the State Key Laboratory of Advanced Electromagnetic Engineering and Technology, School of Electrical and Electronic Engineering, Huazhong University of Science and Technology, Wuhan, 430074, P. R. China (e-mail: wangtao9312@163.com; ccsfm@163.com; liu_tianchang@163.com; zeyun_chao@hust.edu.cn; duanshanxu@hust.edu.cn).

Color versions of one or more of the figures in this article are available online at http://ieeexplore.ieee.org.

Digital Object Identifier 10.1109/TPEL.2019.2944853

PWM method is proposed to reduce the EMI and losses of 2L inverters. However, there are a few literature works on ripple analysis of three-phase three-level rectifier. Thus, it is necessary to analyze the inductor current ripple of Vienna rectifier.

Several papers have concentrated on the current ripple analysis. In [34], the analytical approach is introduced to estimate the RMS value of the current ripple and the method is generalized to an arbitrary level single-phase converter. In [35] and [36], the switching ripple characteristic of five-phase 2L inverter for variable speed motor drive is analyzed and the comparison of current ripple with different modulation methods is implemented. In [37]–[39], the current ripple of three-phase 2L inverter is studied and the analytical expression of amplitude and RMS value of ripple is derived. However, aforementioned papers are not for the three-phase three-level converters and the current ripple of inductor current is different with different circuit topologies. In addition, the inductance variation is not considered.

Grandi *et al*. [40], [41] analyzes the current ripple distribution of three-phase three-level converter, the analytical expression of peak-to-peak current ripple is derived in all sectors with two different methods. Moreover, a comparison of ripple amplitude between 2L and 3L inverter is implemented. However, aforementioned papers have not considered the inductance variation of filter inductor either.

Only a few literature works have considered the inductance variation of filter inductor [42]–[44] when analyzing the current ripple. Wu *et al*. [6]–[10] present the D-Σ control method to compensate the wide value variation of the powder core inductors and apply the method to different systems. In [44], the current ripple of 2L inverter considering the inductance soft saturation of powder cores is analyzed, and the analysis results of current ripple are applied to the variable switching frequency PWM method. However, these papers are for 2L converter or have not presented the brief analytical expression of current ripple peak-to-peak value.

To study the characteristic of current ripple of three-phase Vienna rectifier with powder core inductors, a ripple analysis method considering the inductance variation is proposed. The inductor voltage with inductance variation is calculated by introducing a compensation voltage to compensate for the effect of inductance variation. Then, the analytical expression of peak-to-peak current ripple is derived and an inductor design method is proposed based on analytical expression, which can guide the design of powder core inductor. The rest of the paper is organized as follows: In Section II, the current ripple distribution for three-phase Vienna rectifier with constant inductance is introduced. In Section III, an inductor voltage calculation method with variation of inductance is proposed, and the analytical expression of peak-to-peak current ripple is derived in a fundamental period. Section IV gives the simulation and experimental verifications of the proposed method. In Section V, the conclusions of this article are given.

II. Current Ripple Analysis With Constant Inductance Based on Space Vector Approach

It is complicated to analyze the current ripple of three-phase three-level Vienna rectifier compared with 2L converters. In this section, a method based on space vector approach is proposed to determine the current ripple of Vienna rectifier with constant inductance.

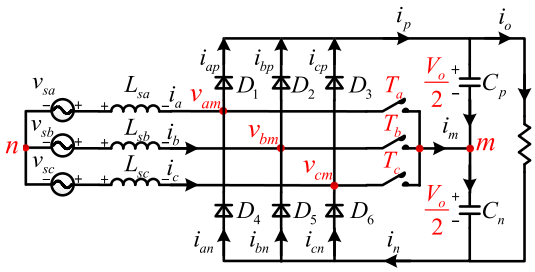

Fig. 1. Topology of three-phase Vienna rectifier.

TABLE I
Terminal Voltage of Vienna Rectifier

Terminal voltage	Conditions	Value of s_x
$v_{xm}=\frac{V_o}{2}s_x$	$i_x>0$ && T_x is off	1
$(x=a,b,c)$	T_x is on	0
	$i_x<0$ && T_x is off	-1

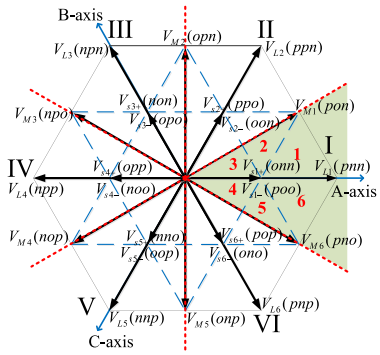

Fig. 2. Space vector diagram of Vienna rectifier.

A. Space Vector Diagram of Vienna Rectifier

The topology of the three-phase Vienna rectifier is shown in Fig. 1. It consists of three four-quadrant semiconductors $T_a - T_c$, six free-wheeling diodes $D_1 - D_6$, two dc bus capacitors, and filter inductors $L_{sa} - L_{sb}$. $v_{am} - v_{cm}$ represent the voltage between terminal of phase legs and midpoint of dc capacitors.

The terminal voltage (v_{am}, v_{bm}, and v_{cm}) of the Vienna rectifier depends on both switching states and polarity of input currents, which can be concluded in Table I. Here, V_o is the output voltage and s_x denotes the states of phase leg.

It can be seen that each phase leg is able to generate three different levels $(V_o/2,\ 0, -V_o/2)$. The space vector diagram of the Vienna rectifier in complex plane is shown in Fig. 2.

The basic space vectors consist of six large vectors $V_{L1} - V_{L6}$, six medium vectors $V_{M1} - V_{M6}$, and twelve redundant small vectors $V_{s1} - V_{s6}$. The lengths of three different vectors are $2V_o/3$, $\sqrt{3}V_o/3$, and $V_o/3$, respectively. It should be mentioned that "p," "o," and "n" represent $V_o/2$, 0, and $-V_o/2$, repectively. The space vector diagram is divided into six main sectors (I–VI) according to the polarity of currents. Each main

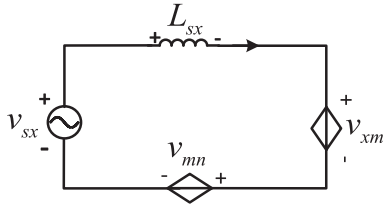

Fig. 3. Single phase equivalent circuit in AC side, where x = *a*, *b*, *c*.

sector consists of six triangles and is divided into six subsectors (1–6) accordingly.

B. Current Ripple Analysis Based on Space Vector Approach

It is necessary to acquire the inductor voltage for current ripple analysis. Based on the single-phase equivalent circuit in Fig. 3, the inductor voltage can be derived as

$$L_{sx}\frac{di_x}{dt} = v_{sx} - (v_{xm} + v_{mn}) = v_{sx} - v_{xn} \qquad (x = a, b, c). \tag{1}$$

Here, v_{sx} is the grid voltage, v_{xm} denotes the terminal voltage of phase leg, v_{mn} represents the middle point voltage referred to mains neutral point (named common-mode voltage), and L_{sx} is the filter inductance. The equivalent series resistance of L_{sx} is neglected. The grid voltage v_{sx} is expressed in (2), where the modulation ratio m is defined as $m = V_{sm}/(V_o/2)$, θ_x represents the phase angle of input voltage

$$v_{sx} = V_{sm}\sin\theta_x = m\frac{V_o}{2}\sin\theta_x, \ x = a, b, c. \tag{2}$$

Assuming that the three-phase inductance is constant and equal, v_{mn} can be derived as

$$v_{mn} = -\frac{1}{3}(v_{am} + v_{bm} + v_{cm}). \tag{3}$$

It can be seen from (1) and (3) that the inductor voltage is calculated by both grid voltage and three-phase terminal voltages, which is determined by basic space vectors. With space vector modulation, the sequence of basic vectors and dwell time can be obtained according to the location of the reference vector V_r. Hence, the characteristic of current ripple in a switching period can be determined by v_s and the location of V_r.

Due to the symmetry of input current, only the phase angle of i_a ranging from 90° to 180° needs to be considered. It is reasonable to neglect the small phase shift between v_s, i_s, and v_r when the rectifier operates with unit power factor. Therefore, the related sectors are illustrated in Fig. 4(a), which consists of sector I-1, I-2, I-3, and the main sector II.

Considering that the reference vector V_r is located at sector I-1, as shown in Fig. 4(b), the nearest basic vectors *poo*, *onn*, *pnn*, and *pon* are selected to synthesis V_r. In order to minimize the switching losses and harmonics, the vector sequence in sector I-1 is arranged symmetrically as *poo-pon-pnn-onn-pnn-pon-poo*. The inductor voltages under different basic vectors and the current ripple in sector I-1 are illustrated in Fig. 5, where i_a stands for the instantaneous value of input current, $\bar{i}_a$ represents

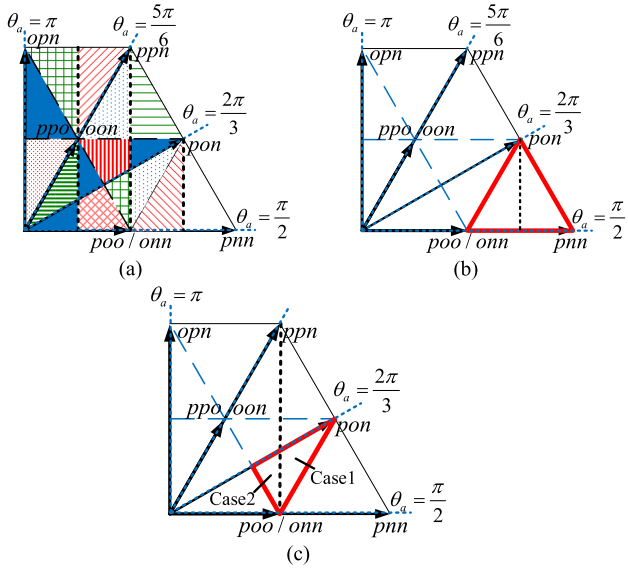

Fig. 4. Related sectors when the phase of i_a is from $\pi/2$ to π.

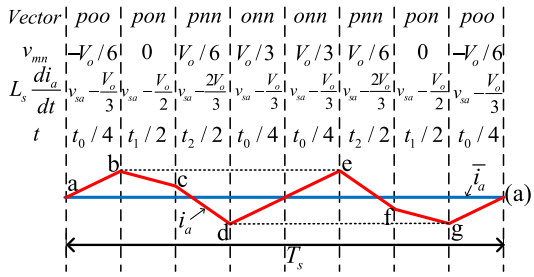

Fig. 5. Current ripple analysis when the reference vector is located in I-1.

the averaged value of i_a in a switching period, and T_s is the switching period.

It should be noticed that v_{sa} is between $V_o/3$ and $V_o/2$ in sector I-1 (only $m < 1$ is considered here). The slope of current segments "a-b," "g-(a)," and "d-e" is positive while the slope of the other current segments is negative. Thus, the maximum value of i_a happens at note "b" while the minimum value of i_a happens at note "g" in the switching period. Then, the peak to peak value of current ripple is derived as

$$\begin{cases} i_{\mathrm{rpp}} = \frac{1}{L_s f_s}\left|(v_{sa} - \frac{V_o}{2})t_1 + (v_{sa} - \frac{2V_o}{3})t_2 + (v_{sa} - \frac{V_o}{3})\frac{t_0}{2}\right| \\ \quad = \frac{V_o}{2L_s f_s}\left|(m\ \sin\theta_a - 1)t_1 + (m\sin\theta_a - \frac{4}{3})t_2 \right. \\ \quad \left. + (m\ \sin\theta_a - \frac{2}{3})\frac{t_0}{2}\right| \\ i_{\mathrm{rpp}}{}^* = i_{\mathrm{rpp}}/(V_o/2L_s f_s) \end{cases} \tag{4}$$

where L_s denotes the filter inductance, f_s is the switching frequency, v_{sa} is expressed in (2), and i^*_{rpp} is defined as the normalized peak to peak current ripple in this paper. The corresponding dwell time of space vectors (t_0, t_1, and t_2) in sector I-1 can be derived based on the principle of volt–second balance [15], [16], as shown in (5). Here, θ_a, θ_b, and θ_c are the phase angles of input voltages

$$t_1 = m\ \sin\theta_b - m\ \sin\theta_c$$

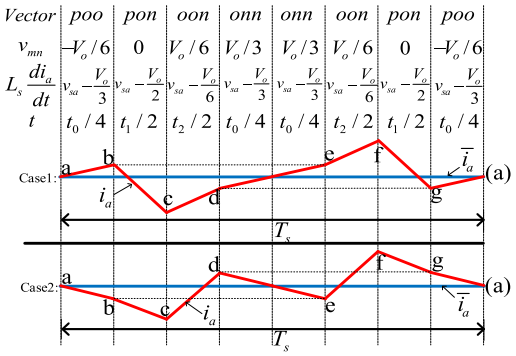

Fig. 6. Current ripple analysis when the reference vector is located in I-2.

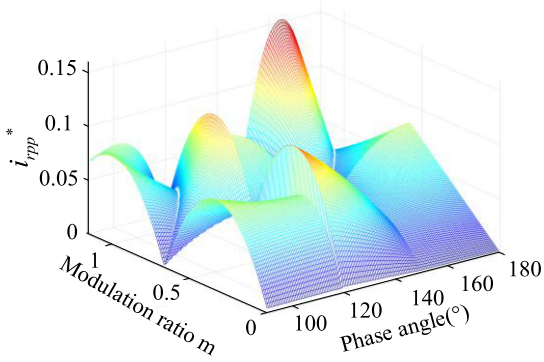

Fig. 7. Current ripple distribution of three-phase Vienna rectifier with constant inductance.

$$t_2 = m\ \sin\theta_a - m\ \sin\theta_b - 1$$
$$t_0 = 1 - t_1 - t_2. \tag{5}$$

Assuming that the reference vector V_r is located at sector I-2, as shown in Fig. 4(c). The nearest vectors *onn*, *poo*, *pon*, and *oon* are selected, the vector sequence in the switching period is *poo-pon-onn-onn-oon-pon-poo*. The inductor voltages and the instantaneous current under different vectors are described in Fig. 6.

It should be mentioned that the slope of the current segments "d-e," "a-b," and "g-a" depends on the location of V_r. When V_r is located at the "case1" of Fig. 4(c), v_{sa} is greater than $V_o/3$, leading to the increase of current in segments "a-b," "d-e," and "g-(a)". In addition, the instantaneous value of i_a at node "b" is equal to the value at node "e," and the value at nodes "d" and "g" are equal as well. Consequently, the maximum value happens at node "f" while the minimum value happens at node "c," as described in "case1" of Fig. 6. Then, the peak to peak current ripple can be expressed as

$$\begin{cases} i_{\rm rpp} = \frac{V_o}{2L_s f_s}\left|(m\ \sin\theta_a - \frac{1}{3})t_2 + (m\ \sin\theta_a - \frac{2}{3})\frac{t_0}{2}\right| \\ {i_{\rm rpp}}^* = i_{\rm rpp}/(V_o/2L_s f_s) \end{cases} \tag{6}$$

where the dwell time of vectors in sector I-2 is derived as

$$t_1 = m\ \sin\theta_a - m\ \sin\theta_c - 1$$
$$t_2 = 1 + m\ \sin\theta_b - m\ \sin\theta_a$$
$$t_0 = 1 - t_1 - t_2. \tag{7}$$

On the contrary, the current in segments "a-b," "d-e," and "g-a" decreases with V_r located in the "case2" of Fig. 4(c). In the same way, the corresponding current ripple is illustrated in the "case2" of Fig. 6, where the maximum and minimum value of i_a is also at node "f" and "c," respectively. Thus, the expression of $i_{\rm rpp}$ is the same as (6). Based on the analysis above, the analytical expression of peak to peak current ripple can be derived in all sectors of Fig. 4(a). Consequently, the distribution of the current ripple of three-phase Vienna rectifier of i_a with constant inductance is illustrated in Fig. 7.

Where $i^*_{\rm rpp}$ represents the normalized value of peak to peak current ripple, the range of modulation ratio is from 0 to 1.15, the phase angle of i_a is from 90° to 180°. It can be seen that the current ripple distribution of three-phase Vienna rectifier is

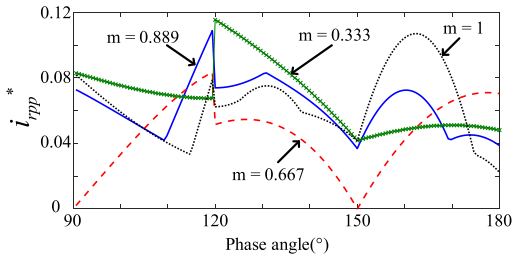

Fig. 8. Current ripple distribution with different *m*.

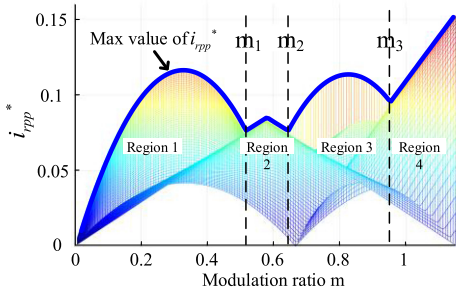

Fig. 9. Max value of peak to peak current ripple versus modulation ratio.

complicated and there exists several local maximum points in the "m–θ_a" plane. To show the current ripple distribution clearly, the waveforms of $i^*_{\rm rpp}$ versus θ_a with $m = 0.333$, 0.667, 0.889, and 1 are shown in Fig. 8.

It can be found that $i^*_{\rm rpp}$ have an obvious discontinuous point at $\theta_a = 120°$, which is the boundary of main sector I and sector II. In addition, the location of the maximum ripple in a fundamental period is related to the modulation ratio *m*. For example, maximum value of $i^*_{\rm rpp}$ happens at left side of 120° with $m = 0.667$, the max peak to peak value occurs at right side of 120° with $m = 0.333$, and the maximum value occurs between 160° and 165° with $m = 1$. The side view of the current distribution in Fig. 8 is shown in Fig. 9, where the envelope line reflects the relationship between m and the maximum value of $i^*_{\rm rpp}$ in a fundamental period. It should be mentioned that the envelope line in Fig. 9 is useful to determine the maximum current ripple of three-level rectifier with constant inductance, which is the basis for filter inductor design. Although the analysis above is based on space

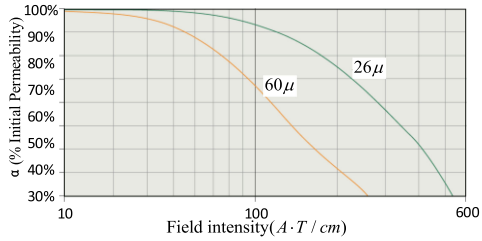

Fig. 10. Curve of saturation coefficient versus field intensity.

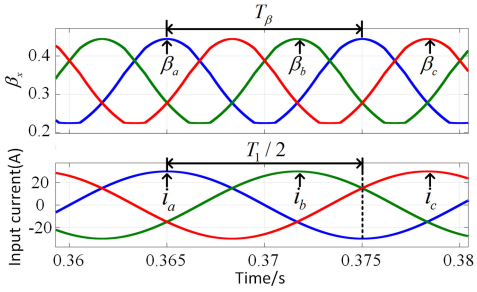

Fig. 11. Simulation waveform of $\beta_a - \beta_c$ with sinusoidal input currents.

vector modulation with unity power factor, the ripple analysis method can be extended to three-phase three-level rectifier with other modulation methods and power factors.

III. Current Ripple Analysis Considering Inductance Variation of Powder Core Inductor

The powder core inductors have been widely applied due to the significant reduction in size. However, the inductance variation of powder core inductors makes it more complicated to determine the current ripple distribution of three-phase three-level rectifiers. In this section, the current ripple with the inductance variation of powder core inductor is analyzed and the analytical expression of peak-to-peak current ripple is derived.

A. Characteristics of Powder Core Inductors

The permeability of powder core inductors has a significant reduction with the increase of the magnetic field intensity. Thus, the inductance will decrease with the growth of the absolute value of inductor current. For convenience, the inductance of powder core inductor is defined as

$$L_{sx} = \alpha_x L_s \ (x = a, b, c) \tag{8}$$

where L_s represents the inductance when the inductor current is zero and is called the static inductance in this article. α_x is defined as saturation coefficient, which is related to the materials of powder core. The common materials used for powder core are "Fe-Si-Al," "Fe-Si," "Fe-Ni," and "Fe-Ni-Mo," the "Fe-Si" is used for filter inductor in this article. The curve of saturation coefficient versus magnetic field intensity is provided by the manufactory [45], as shown in Fig. 10. It can be seen that α_x is reduced to less than 30% with the increase of intensity, indicating that the inductance of powder core inductors varies widely with sinusoidal inductor current.

B. Proposed Inductor Voltage Calculation Method With Inductance Variation

Considering the inductance variation of powder core inductor, the mathematical model in ac side is modified in (9), where α_a, α_b, and α_c are the saturation coefficients of three-phase inductors

$$v_{sa} = \alpha_a L_s \frac{di_a}{dt} + v_{am} + v_{mn}$$

$$v_{sb} = \alpha_b L_s \frac{di_b}{dt} + v_{bm} + v_{mn}$$

$$v_{sc} = \alpha_c L_s \frac{di_c}{dt} + v_{cm} + v_{mn}. \tag{9}$$

In particular, v_{mn} is more complicated due to the unequal three-phase instantaneous inductance [44]. Based on (9), v_{mn} can be derived in (10), where α_{com} is expressed in (11)

$$v_{mn} = \frac{\alpha_b\alpha_c(v_{sa} - v_{am}) + \alpha_a\alpha_c(v_{sb} - v_{bm}) + \alpha_a\alpha_b(v_{sc} - v_{cm})}{{\alpha_{com}}^2} \tag{10}$$

$$\alpha_{com} = \sqrt{\alpha_b\alpha_c + \alpha_a\alpha_c + \alpha_a\alpha_b}. \tag{11}$$

For convenience, the variables β_a, β_b, and β_c are defined as

$$\beta_a = \frac{\alpha_b\alpha_c}{{\alpha_{com}}^2},\ \beta_b = \frac{\alpha_a\alpha_c}{{\alpha_{com}}^2},\ \beta_c = \frac{\alpha_a\alpha_b}{{\alpha_{com}}^2}. \tag{12}$$

The calculation of $\beta_a - \beta_c$ is necessary to obtain the inductor voltage, which is the basis for current ripple analysis. However, it is almost impossible to obtain the analytical expression of $\beta_a - \beta_c$ based on the curve in Fig. 10. By observing the expression in (12), some key characteristics of $\beta_a - \beta_c$ are summarized as follows.

1) $\beta_a - \beta_c$ swing at twice the fundamental frequency, because the saturation coefficients $\alpha_a - \alpha_c$ are the function of absolute value of inductor currents.
2) The averaged value of $\beta_a - \beta_c$ is 1/3 due to the symmetry of three-phase currents.
3) The maximum value of $\beta_a - \beta_c$ happens at the peak of input current while the minimum value occurs at the zero point of input current.

The simulation waveforms of $\beta_a - \beta_c$ with sinusoidal three-phase input currents are shown in Fig. 11.

Fig. 11 shows that $\beta_a - \beta_c$ swing at twice the fundamental frequency with the averaged value of 1/3. Therefore, $\beta_a - \beta_c$ can be approximated with dc component adding twice frequency

component as

$$\beta_a \approx \frac{1}{3} + \beta_m \sin\left(2\theta_a - \frac{\pi}{2}\right)$$
$$\beta_b \approx \frac{1}{3} + \beta_m \sin\left(2\theta_b - \frac{\pi}{2}\right)$$
$$\beta_c \approx \frac{1}{3} + \beta_m \sin\left(2\theta_c - \frac{\pi}{2}\right). \quad (13)$$

$\theta_a - \theta_c$ are the phase angles of input currents, β_m denotes the amplitude of twice frequency component, which can be calculated as

$$\beta_m = \beta_a|_{\theta_a=\frac{\pi}{2}} - \frac{1}{3} = \frac{\alpha_b\alpha_c}{{\alpha_{com}}^2}\bigg|_{\theta_a=\frac{\pi}{2}} - \frac{1}{3}. \quad (14)$$

Still, it is very hard to calculate β_m with Fig. 10. Thus, a simple linear method of saturation coefficient is implemented. The curve of $\alpha_a - \alpha_c$ is approximated with a straight line, as expressed in

$$\alpha_a \approx 1 - \frac{1-\alpha_{\min}}{I_m}|i_a| = 1 - (1-\alpha_{\min})|\sin\theta_a|$$
$$\alpha_b \approx 1 - \frac{1-\alpha_{\min}}{I_m}|i_b| = 1 - (1-\alpha_{\min})|\sin\theta_b|$$
$$\alpha_c \approx 1 - \frac{1-\alpha_{\min}}{I_m}|i_c| = 1 - (1-\alpha_{\min})|\sin\theta_c| \quad (15)$$

where $\alpha_{\min}$ is the minimum saturation coefficient when the input current reaches the peak value. Substituting (15) into (14), the analytical expression of β_m is derived as

$$\beta_m = \frac{1+\alpha_{\min}}{1+5\alpha_{\min}} - \frac{1}{3} = \frac{2-2\alpha_{\min}}{3+15\alpha_{\min}}. \quad (16)$$

Combining (10), (13), and (16), the expression of v_{mn} with inductance variation is obtained, as shown in (17). Here, $\mathbf{C}$ is expressed in (18), v_{mn1} is expressed in (19), and represents common-mode voltage with constant inductance, Δv_{mn} is called the compensation voltage

$$\begin{aligned} v_{mn} =& -\frac{1}{3}(v_{am}+v_{bm}+v_{cm}) \\ & -\beta_m C\left[(v_{sa}-v_{am})\ (v_{sb}-v_{bm})\ (v_{sc}-v_{cm})\right]^T \\ =& v_{mn1} + \Delta v_{mn} \end{aligned} \quad (17)$$

$$C = \left[\cos 2\theta_a\ \cos 2\theta_b\ \cos 2\theta_c\right] \quad (18)$$

$$v_{mn1} = -\frac{1}{3}(v_{am}+v_{bm}+v_{cm}). \quad (19)$$

It can be seen that the common-mode voltage with inductance variation (v_{mn}) can be calculated by common mode voltage with constant inductance (v_{mn1}) adding the compensation voltage Δv_{mn}. Deriving from (17), Δv_{mn} is simplified to

$$\begin{aligned} \Delta v_{mn} =& -\beta_m C\left[(v_{sa}-v_{am})\ (v_{sb}-v_{bm})\ (v_{sc}-v_{cm})\right]^T \\ =& \frac{V_o}{2}\left(-\frac{3}{2}\beta_m m\ \sin 3\theta_a + \beta_m C S^T\right) \end{aligned} \quad (20)$$

where $S^T = [s_a\ \ s_b\ \ s_c]^T$ represents the states of phase legs, s_x = "1," "0," "−1" denote that the terminal voltages are positive, zero, and negative, respectively. By observing (20),

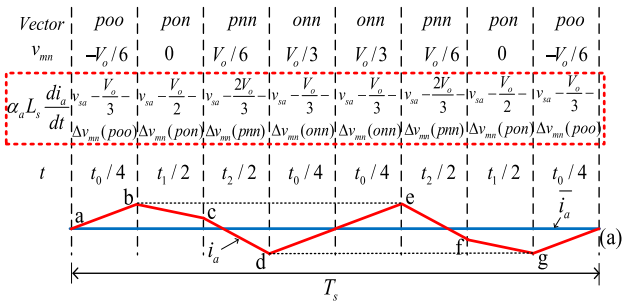

Fig. 12. Current ripple analysis with inductance variation of powder core inductor when v_r is located in sector I-1.

the compensation voltage Δv_{mn} is determined by basic vectors, all phase angles $\theta_a - \theta_c$ and $\alpha_{\min}$. Finally, the inductor voltage with inductance variation is derived as

$$\begin{aligned} \alpha_a L_s \frac{di_a}{dt} &= v_{sa} - v_{am} - (v_{mn1} + \Delta v_{mn}) \\ &= v_{sa} - v_{an1} - \Delta v_{mn}. \end{aligned} \quad (21)$$

Compared with (1), the compensation voltage Δv_{mn} is introduced to compensate for the effect of inductance variation on inductor voltage. The inductor voltage with the inductance variation of powder core inductor is related to not only the basic space vector and input voltage but also the minimum saturation coefficient $\alpha_{\min}$ and all the phase angles $\theta_a - \theta_c$.

C. Current Ripple Analysis Considering the Inductance Variation of Powder Core Inductor

By introducing the compensation voltage Δv_{mn}, the inductor voltage with inductance variation can be calculated analytically based on (16), (20), and (21). Accordingly, the current ripple with inductance variation of powder core inductor can be determined. Assuming that the reference voltage v_r is located at sector I-1, as shown in Fig. 4(b), the inductor voltage and corresponding current ripple are illustrated in Fig. 12.

It can be found that the compensation voltages under different space vectors are added to the inductor voltage. Still, the maximum value of i_a happens at the node "b" while the minimum value of i_a happens at node "g" in sector I-1. Thus, the peak-to-peak current ripple in a switching period in sector I-1 can be expressed as

$$\begin{cases} i_{\text{rpp}} = \frac{V_o}{2L_s f_s}\frac{1}{\alpha_a} \left| \begin{array}{l} (m\ \sin\theta_a - 1 - \Delta v_{mn}(pon))t_1 \\ +(m\ \sin\theta_a - \frac{4}{3} - \Delta v_{mn}(pnn))t_2 \\ +(m\ \sin\theta_a - \frac{2}{3} - \Delta v_{mn}(onn))\frac{t_0}{2} \end{array} \right| \\ {i_{\text{rpp}}}^* = i_{\text{rpp}}/(V_o/2L_s f_s) \end{cases} \quad (22)$$

where the dwell time of space vector t_0, t_1, and t_2 in sector I-1 are given in (5). The compensation voltages $\Delta v_{mn}(pon)$,$\Delta v_{mn}(pnn)$, and $\Delta v_{mn}(onn)$ are calculated based on (20) and normalized by $V_o/2$. The saturation coefficient is calculated with (15). Similarly, the analytical expressions of peak-to-peak current ripple in other sectors can be derived using the same method. The current ripple distribution of three-phase

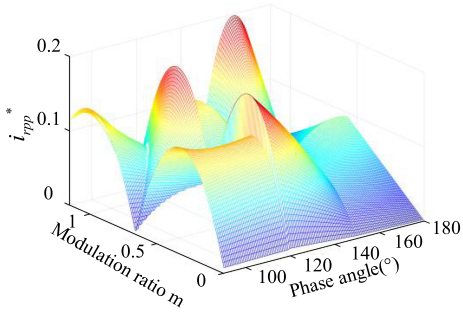

Fig. 13. Current ripple distribution of three-phase three-level rectifier when the minimum saturation coefficient $\alpha_{\min} = 0.5$.

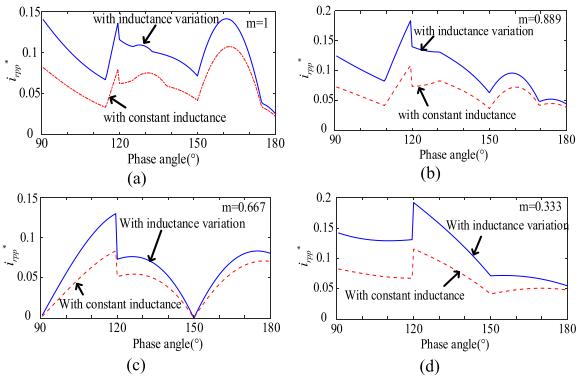

Fig. 14. Comparison of $i^*_{\rm rpp}$ with different m when the minimum saturation coefficient $\alpha_{\min} = 0.5$. (a) $m = 1$. (b) $m = 0.889$. (c) $m = 0.667$. (d) $m = 0.333$.

Vienna rectifier with powder core inductor ($\alpha_{\min} = 0.5$) is illustrated in Fig. 13, where $i^*_{\rm rpp}$ represents the normalized value of peak to peak current ripple and the range of m is from 0 to 1.15.

Only the phase angle of i_a from 90° to 180° is analyzed due to the symmetry of three-phase currents and several peaks also exist in the "$m-\theta_a$" plane. To compare current ripple with constant inductance, the curves of $i^*_{\rm rpp}$ with different modulation ratios when the minimum saturation coefficient $\alpha_{\min} = 0.5$ are shown in Fig. 14. It shows that the current ripple distribution in a fundamental period varies with m. In addition, the peak-to-peak value of current ripple with inductance variation is much higher due to the significant decrease of inductance. It should also be emphasized that the peak-to-peak current ripple in Figs. 13 and 14 is calculated with $\alpha_{\min} = 0.5$ and the ripple distribution will be different under other values of $\alpha_{\min}$.

D. Design of Powder Core Inductor Based on Maximum Current Ripple Amplitude

The maximum peak-to-peak current ripple in a fundamental period is usually limited to a certain value [22]–[24], which is the basis for filter inductor design. The side view of Fig. 13 is shown in Fig. 15, where the envelope line reflects the curve of maximum peak-to-peak current ripple versus m with $\alpha_{\min} = 0.5$.

It should be mentioned that the phase angle where the maximum ripple happens is determined by the modulation ratio

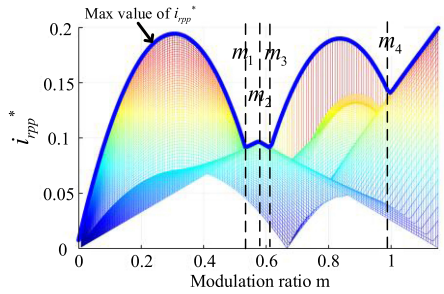

Fig. 15. Max value of peak-to-peak current ripple versus m with $\alpha_{\min} = 0.5$.

TABLE II
REGIONS AND ANGLE WHERE MAXIMIUM RIPPLE HAPPENS

Modulation ratio	Regions and phase where maximum ripple happens	Maximum peak-to-peak value of current ripple
$0 < m < m_1$	Region1, $\theta_a = 120°$	$i^*_{Max1} = i^*_{rpp}(r1, 120°)$
$m_1 < m < m_2$	Region2, $\theta_a = 180°$	$i^*_{Max2} = i^*_{rpp}(r2, 180°)$
$m_2 < m < m_3$	Region3, $\theta_a = 180°$	$i^*_{Max3} = i^*_{rpp}(r3, 180°)$
$m_3 < m < m_4$	Region4, $\theta_a = 120°$	$i^*_{Max4} = i^*_{rpp}(r4, 120°)$
$m_4 < m < 1$	Region5, $\theta_a = 90°$	$i^*_{Max5} = i^*_{rpp}(r5, 90°)$
$1 < m < 1.15$	Region3, $\theta_a = 160°$	$i^*_{Max6} = i^*_{rpp}(r3, 160°)$

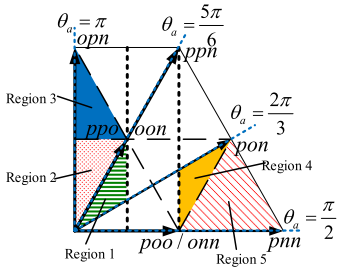

Fig. 16. Possible regions where the maximum current ripple happens.

m and the minimum saturation coefficient $\alpha_{\min}$. The region and phase angle where maximum current ripple happens can be concluded in Table II, where $i^*_{\rm Max\,1} - i^*_{\rm Max\,6}$ represent the analytical expression of max current ripple in region1–region5 of Fig. 16.

For example, when $m_3 < m < m_4$, the maximum peak-to-peak current ripple occurs at 120° with V_r located in region4 of Fig. 16 and $i^*_{\rm rpp}(r4,\ 120°)$ in Table II represents the analytical expression of the $i^*_{\rm rpp}$ in region4 with the phase angle of 120°, which is the function of modulation ratio and minimum saturation coefficient $\alpha_{\min}$.

However, the values of $m_1 - m_4$ are different under different $\alpha_{\min}$, the maximum value of $i^*_{\rm Max\,1} - i^*_{\rm Max\,6}$ have to be found to determine the maximum peak-to-peak current ripple with different m. Consequently, the required static inductance of powder core inductor can be calculated in

$$L_s > \frac{V_o}{2 f_s \Delta I} i^*_{\max} \tag{23}$$

where L_s denotes the static inductance, f_s is the switching frequency, V_o represents the output voltage, ΔI stands for the maximum allowable peak-to-peak current ripple, and $i^*_{\max}$ is the maximum value of $i^*_{\rm Max\,1} - i^*_{\rm Max\,6}$. The design flow chart of the powder core inductor for three-phase Vienna rectifier is

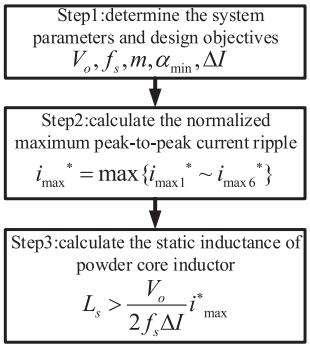

Fig. 17. Proposed design method of powder core inductor.

TABLE III
PARAMETERS OF POWDER CORE INDUCTOR

Parameter	Value
Material	Fe-Si
Permeability	60 μ
Dimension OD × ID × HT	46.7 mm × 24.1 mm × 18 mm
Path length	10.7 cm
Inductance factor	124 nH/T^2
Winding turns	52
Static inductance	340 μH

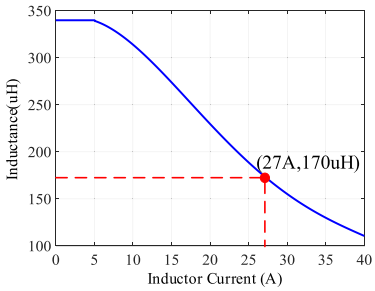

Fig. 18. Inductance versus the absolute value of inductor current.

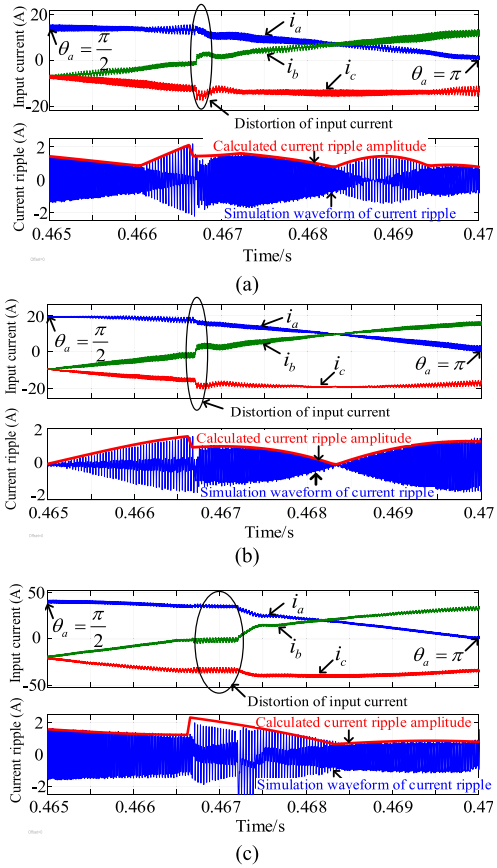

Fig. 19. Simulation waveforms of input currents and current ripple from $\theta_a = 90°$ to $\theta_a = 180°$. (a) $m = 0.889$ ($V_{sm} = 311$ V, $V_o = 700$ V). (b) $m = 0.667$ ($V_{sm} = 233$ V, $V_o = 700$ V). (c) $m = 0.333$ ($V_{sm} = 117$ V, $V_o = 700$ V).

proposed, as described in Fig. 17. Based on the proposed design method, the designed static inductance and minimum saturation coefficient powder core inductor can be determined.

The detailed design parameters of powder core inductors are shown in Table III, where the material is "Fe-Si," the part number is "78 439" from the magnetics. $\alpha_{\min}$ is 0.5 at the peak of current, ΔI is designed at 20% of nominal peak current, the switching frequency is 30 kHz, and the output voltage is 700 V.

Based on the design parameters in Table III and Fig. 10, the waveform of the inductance versus the inductor current can be derived in Fig. 18. It can be seen that the peak value of the input current at normal load is 27 A and the corresponding inductance is half the static inductance (170 μH).

IV. SIMULATION AND EXPERIMENTAL RESULTS

A. Simulation Verification With Constant Inductor

To validate the correctness of the current ripple analysis with constant inductance in Section II, simulations are carried out for a three-phase Vienna rectifier. The key simulation parameters are as follows: the output voltage is 700 V, the switching frequency is 30 kHz, and the inductance is 300 μH. In order to verify the analytical expressions of peak-to-peak current ripple at all sectors in Fig. 4, the simulations with m = 0.889 ($V_{sm} = 311$ V, $V_o = 700$ V), m = 0.667 ($V_{sm} = 233$ V, $V_o = 700$ V), and m = 0.333 ($V_{sm} = 117$ V, $V_o = 700$ V) are implemented, respectively. The simulation waveforms of input current and corresponding current ripple in a quarter of fundamental period (from $\theta_a = 90°$ to $\theta_a = 180°$) are illustrated in Fig. 19, where i_a, i_b, and i_c are three-phase input currents and the fundamental frequency is 50 Hz. The simulated current ripple is the error between the instantaneous value i_a and the averaged value in a switching period $\bar{i}_a$. The calculated current ripple is half of $i_{\rm rpp}$, which is obtained by the analytical expression derived in Section II.

It can be seen that the calculated current ripple amplitude envelopes the simulation waveform of the current ripple, which means that the calculated peak-to-peak current ripple is close to the simulation results in all sectors shown in Fig. 4. However, there exists a little error between calculated and simulation results near the zero-crossing of i_b, which is caused by the inherent current distortion around the zero-crossing point of Vienna rectifier [17]–[20].

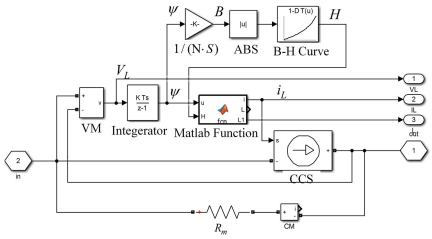

Fig. 20. Simulated diagram of powder core inductor.

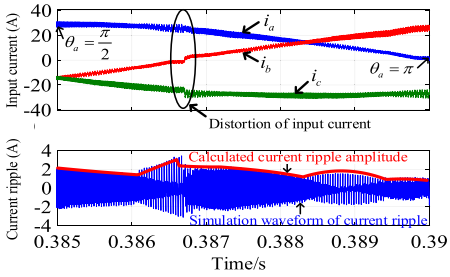

Fig. 21. Simulated current ripple with powder core inductors.

B. Simulation Verification With Powder Core Inductor

Three-phase Vienna rectifier with powder core is simulated in Matlab/Simulink, and the powder core inductor is modeled by the controlled current source based on the inductor parameters, as illustrated in Fig. 20.

The simulated current ripple of the three-phase Vienna rectifier with powder core inductor is shown in Fig. 21, where the RMS value of input line-to-line voltage is 380 V, the output voltage is 700 V (the modulation ratio is 0.889), the switching frequency is 30 kHz and the load is 39 Ω. In addition, the powder core inductor model in Fig. 20 is used and the inductance variation is from 340 μH to 170 μH.

It can be seen that the amplitude of the simulated current ripple is close to the calculated results. However, there exists a little error between the simulation and calculated results, because there exists inherent current distortion at zero-crossing points and the value of common-mode voltage with inductance variation is calculated approximately.

C. Experimental Verification With Powder Core Inductor

The expression of peak-to-peak current ripple considering the inductance variation is verified by a three-phase Vienna rectifier prototype with powder core inductors, as shown in Fig. 22.

The experiment parameters of the prototype are shown in Table IV. The nominal power is 12.5 kW, the RMS value of input line-to-line voltage is 380 V, the peak current at nominal load is 27 A, the inductance of powder core inductors varies from 170 μH to 340 μH at the nominal load, and the switching frequency is 30 kHz. The detailed design parameters of powder core inductor are shown in Table III.

The experimental waveforms with powder core inductor are illustrated in Fig. 23, where i_a– i_c represent the input currents and v_o is the output voltage. The output voltage is 700 V in steady state and the peak value of input currents is 27 A. Fig. 23(c) and

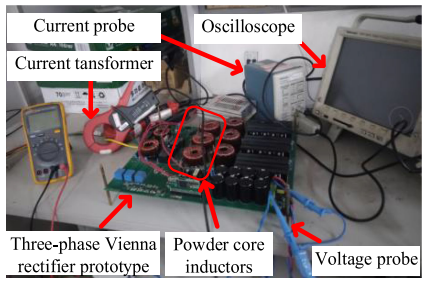

Fig. 22. Three-phase Vienna rectifier prototype.

TABLE IV
DESIGN PARAMETERS OF PROTOTYPE

Symbol	Quantity	Values
P_n	Nominal power	12.5 kW
V_s	Nominal grid voltage	380 V(RMS value)
V_o	Output voltage	700 V
I_m	Peak current	27 A
L_{sx}	Inductance	170~340 μH
C_p, C_n	DC bus capacitance	880 μF
f_s	Switching frequency	30 kHz
f_0	Fundamental frequency	50 Hz
STW48NM60N	Power MOSFET	$V_{DS} = 600\,V$, $I_D = 44A, R_{DS} = 55\,m\Omega$
APT30DQ120B	Ultrafast recovery diode	$V_R = 1200\,V$, $I_F = 30A, V_F = 2.5\,V$

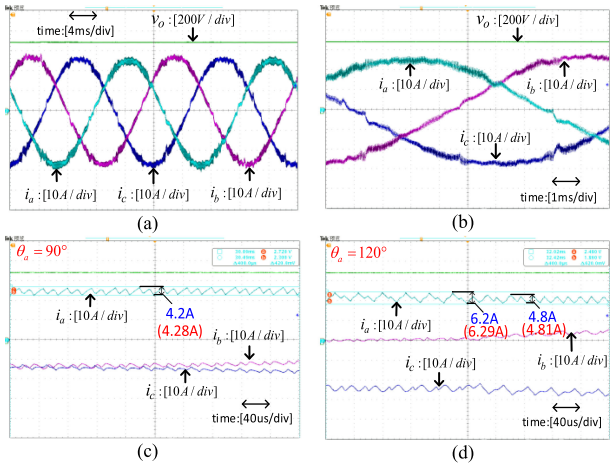

Fig. 23. Experimental waveforms. (a) Input currents in a fundamental period. (b) Input currents in half a fundamental period. (c) Details of i_a at $\theta_a = 90°$. (d) Details of i_a at $\theta_a = 120°$.

(d), respectively, show the details of input current at $\theta_a = 90°$ and $\theta_a = 120°$, where the peak-to-peak values of input currents are measured by oscilloscope and the value in the parentheses are calculated based on the analytical expression. The experimental value of peak-to-peak current ripple at 90° and 120° are close to theoretical results. In addition, Fig. 23(d) shows that the peak-to-peak current ripple changes suddenly at $\theta_a = 120°$, which is consistent with the theoretical analysis.

The comparison of experimental current ripple and the calculated current ripple amplitude is shown in Fig. 24, where the waveform of i_a from 90° to 180° is presented. The experimental waveform of current ripple is obtained by $i_a - \bar{i}_a$ based on the experimental data. The calculated current ripple amplitude is

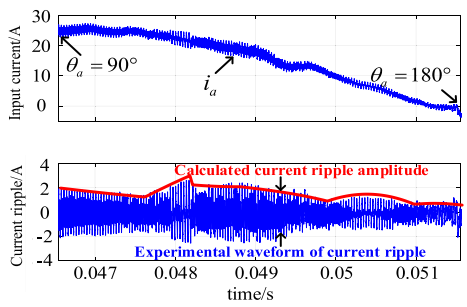

Fig. 24. Experimental current ripple with powder core inductor from $\theta_a = 90°$ to $\theta_a = 180°$.

half of i_{rpp}, which is obtained based on the analytical expression in Section III. It can be observed that the calculated ripple amplitude nearly envelopes the experimental waveform of current ripple, which validates the correctness of the current ripple analysis with inductance variation of powder core inductor.

However, there exists little errors between the real and calculated value of the current ripple amplitude. The possible reasons are as follows.

1) $\beta_a - \beta_c$ and saturation coefficients $\alpha_a - \alpha_c$ are calculated approximately.
2) The inherent zero-crossing distortion of the input current of Vienna rectifier will occur with space vector modulation.
3) The system parameters and experimental conditions may be different from the ideal value.
4) Measurement errors caused by oscilloscope and current probe exist.

V. Conclusion

The inductance variation of powder core inductor makes it complicated to determine the ripple distribution of the three-phase three-level Vienna rectifier. This article presents the current ripple analysis method for three-phase Vienna rectifier considering the inductance variation of the powder core inductor. An inductor voltage calculation method with variation of inductance is proposed. Then, the analytical expression of peak-to-peak current ripple with inductance variation is derived, which is useful for modulation method optimization, loss estimation, and powder core inductor design. In addition, a design method of powder core inductor is proposed based on the current ripple analysis with inductance variation. Finally, the simulation and experimental results of current ripple amplitude are close to the theoretical value, which validates the correctness of current ripple analysis in this article.

References

[1] J. W. Kolar and T. Friedli, "The essence of three-phase PFC rectifier systems—Part I," *IEEE Trans. Power Electron.*, vol. 28, no. 1, pp. 176–198, Jan. 2013.

[2] T. Friedli, M. Hartmann, and J. W. Kolar, "The essence of three-phase PFC rectifier systems—Part II," *IEEE Trans. Power Electron.*, vol. 29, no. 2, pp. 543–560, Feb. 2014.

[3] J. Imaoka, K. Okamoto, M. Shoyama, Y. Ishikura, M. Noah, and M. Yamamoto, "Modeling, magnetic design, simulation methods, and experimental evaluation of various powder cores used in power converters considering their DC superimposition characteristics," *IEEE Trans. Power Electron.*, vol. 34, no. 9, pp. 9033–9051, Sep. 2019.

[4] M. S. Rylko, B. J. Lyons, J. G. Hayes, and M. G. Egan, "Revised magnetics performance factors and experimental comparison of high-flux materials for high-current DC–DC inductors," *IEEE Trans Power Electron.*, vol. 26, no. 8, pp. 2112–2126, Aug. 2011.

[5] Magnetcs Powder Core Shapes Bulletin. [Online]. Available: www.mag-inc.com.cn. Accessed: May 12, 2019.

[6] T. F. Wu, K. H. Sun, C. L. Kuo, and C. H. Chang, "Predictive current controlled 5-kW single-phase bidirectional inverter with wideinductance variation for DC-microgrid applications," *IEEE Trans. Power Electron.*, vol. 25, no. 12, pp. 3076–3084, Dec. 2010.

[7] T. F. Wu, C. Chang, L. Lin, Y. Chang, and Y. Chang, "Two-phase modulated digital control for three-phase bidirectional inverter with wide inductance variation," *IEEE Trans. Power Electron.*, vol. 28, no. 4, pp. 1598–1607, Apr. 2013.

[8] T. F. Wu, C. H. Chang, L. C. Lin, G. R. Yu, and Y. R. Chang, "A D-Σ digital control for three-phase inverter to achieve active and reactive power injection," *IEEE Trans. Ind. Electron.*, vol. 61, no. 8, pp. 3879–3890, Aug. 2014.

[9] T. F. Wu, L. C. Lin, N. Yao, Y. K. Chen, and Y. C. Chang, "Extended application of D-Σ digital control to a single-phase bidirectional inverter with an LCL filter," *IEEE Trans. Power Electron.*, vol. 30, no. 7, pp. 3903–3911, Jul. 2015.

[10] T. Wu, H. Hsieh, C. Chang, L. Lin, and Y. Chang, "Improvement of control law derivation and region selection for D-Σ digital control," *IEEE Trans. Ind. Electron.*, vol. 62, no. 10, pp. 6042–6050, Oct. 2015.

[11] D. O. Boillat, F. Krismer, and J. W. Kolar, "EMI filter volume minimization of a three-phase, three-level T-Type PWM converter system," *IEEE Trans. Power Electron.*, vol. 32, no. 4, pp. 2473–2480, Apr. 2017.

[12] M. Hartmann, H. Ertl, and J. W. Kolar, "EMI filter design for a 1 MHz, 10 kW three-phase/level PWM rectifier," *IEEE Trans Power Electron.*, vol. 26, no. 4, pp. 1192–1204, Apr. 2011.

[13] H.-W. Kim, B.-C. Yoon, K.-Y. Cho, B.-K. Lim, and S.-S. Hwang, "Single carrier wave comparison PWM for Vienna rectifier and consideration for DC-link voltage unbalance of offset voltage effects," in *Proc. 33rd IEEE Int. Telecommun. Energy Conf.*, 2011, pp. 1–6.

[14] R. Lai, F. Wang, R. Burgos, D. Boroyevich, D. Jiang, and D. Zhang, "Average modeling and control design for VIENNA-type rectifiers considering the DC-link voltage balance," *IEEE Trans. Power Electron.*, vol. 24, no. 11, pp. 2509–2522, Nov. 2009.

[15] R. Burgos, R. Lai, Y. Pei, F. Wang, D. Boroyevich, and J. Pou, "Space vector modulator for Vienna-type rectifiers based on the equivalence between two and three-level converters: A carrier-based implementation," *IEEE Trans. Power Electron.*, vol. 23, no. 4, pp. 1888–1898, Jul. 2008.

[16] L. Hang, B. Li, M. Zhang, Y. Wang, and L. M. Tolbert, "Equivalence of SVM and carrier-based PWM in three-phase/wire/level Vienna rectifier and capability of unbalanced-load control," *IEEE Trans. Ind. Electron.*, vol. 61, no. 1, pp. 20–8, Jan. 2014,

[17] L. Dalessandro, S. D. Round, U. Drofenik, and J. W. Kolar, "Discontinuous space-vector modulation for three-level PWM rectifiers," *IEEE Trans. Power Electron.*, vol. 23, no. 2, pp. 530–542, Mar. 2008.

[18] J. Lee and K. Lee, "Carrier-based discontinuous PWM method for Vienna rectifiers," *IEEE Trans. Power Electron.*, vol. 30, no. 6, pp. 2896–2900, Jun. 2015.

[19] J. Lee and K. Lee, "Performance analysis of carrier-based discontinuous PWM method for Vienna rectifiers with neutral-point voltage balance," *IEEE Trans. Power Electron.*, vol. 31, no. 6, pp. 4075–4084, Jun. 2016.

[20] J. Lee and K. Lee, "A novel carrier-based PWM method for Vienna rectifier with a variable power factor," *IEEE Trans. Ind. Electron.*, vol. 63, no. 1, pp. 3–12, Jan. 2016.

[21] M. Liserre, F. Blaabjerg, and S. Hansen, "Design and control of an LCL-filter-based three-phase active rectifier," *IEEE Trans. Ind. Appl.*, vol. 41, no. 5, pp. 1281–1291, Sep./Oct. 2005.

[22] D. O. Boillat, F. Krismer, and J. W. Kolar, "EMI filter volume minimization of a three-phase, three-level T-type PWM converter system," *IEEE Trans. Power Electron.*, vol. 32, no. 4, pp. 2473–2480, Apr. 2017.

[23] J. Muhlethaler, M. Schweizer, R. Blattmann, J. W. Kolar, and A. Ecklebe, "Optimal design of LCL harmonic filters for three-phase PFC rectifiers," *IEEE Trans. Power Electron.*, vol. 28, no. 7, pp. 3114–3125, Jul. 2013.

[24] Y. Jiao and F. C. Lee, "LCL filter design and inductor current ripple analysis for a three-level NPC grid interface converter," *IEEE Trans. Power Electron.*, vol. 30, no. 9, pp. 4659–4668, Sep. 2015.

[25] S. Barg, K. Ammous, H. Mejbri, and A. Ammous, "An improved empirical formulation for magnetic core losses estimation under nonsinusoidal induction," *IEEE Trans. Power Electron.*, vol. 32, no. 3, pp. 2146–2154, Mar. 2017.
[26] J. Muhlethaler, J. Biela, J. W. Kolar, and A. Ecklebe, "Improved core-loss calculation for magnetic components employed in power electronic systems," *IEEE Trans. Power Electron.*, vol. 27, no. 2, pp. 964–973, Feb. 2012.
[27] J. Muhlethaler, M. Schweizer, R. Blattmann, J. W. Kolar, and A. Ecklebe, "Optimal design of LCL harmonic filters for three-phase PFC rectifiers," *IEEE Trans. Power Electron.*, vol. 28, no. 7, pp. 3114–3125, Jul. 2013.
[28] R. Ghosh and G. Narayanan, "Control of three-phase, four-wire PWM rectifier," *IEEE Trans. Power Electron.*, vol. 23, no. 1, pp. 96–106, Jan. 2008.
[29] G. Narayanan, D. Zhao, H. K. Krishnamurthy, R. Ayyanar, and V. T. Ranganathan, "Space vector based hybrid PWM techniques for reduced current ripple," *IEEE Trans. Ind. Electron.*, vol. 55, no. 4, pp. 1614–1627, Apr. 2008.
[30] D. Zhao, V. S. S. P. K. Hari, G. Narayanan, and R. Ayyanar, "Space-vector-based hybrid pulsewidth modulation techniques for reduced harmonic distortion and switching loss," *IEEE Trans. Power Electron.*, vol. 25, no. 3, pp. 760–774, Mar. 2010.
[31] T. T. Nguyen, N. Nguyen, and N. R. Prasad, "Novel eliminated common-mode voltage PWM sequences and an online algorithm to reduce current ripple for a three-level inverter," *IEEE Trans. Power Electron.*, vol. 32, no. 10, pp. 7482–7493, Oct. 2017.
[32] X. Mao, R. Ayyanar, and H. K. Krishnamurthy, "Optimal variable switching frequency scheme for reducing switching loss in single-phase inverters based on time-domain ripple analysis," *IEEE Trans. Power Electron.*, vol. 24, no. 4, pp. 991–1001, Apr. 2009.
[33] D. Jiang and F. Wang, "Variable switching frequency PWM for three-phase converters based on current ripple prediction," *IEEE Trans. Power Electron.*, vol. 28, no. 11, pp. 4951–4961, Nov. 2013.
[34] B. Reznikov, M. Srndovic, Y. L. Familiant, G. Grandi, and A. Ruderman, "Simple time averaging current quality evaluation of a single-phase multilevel PWM inverter," *IEEE Trans. Ind. Electron.*, vol. 63, no. 6, pp. 3605–3615, Jun. 2016.
[35] D. Dujic, M. Jones, and E. Levi, "Analysis of output current ripple RMS in multiphase drives using space vector approach," *IEEE Trans. Power Electron.*, vol. 24, no. 8, pp. 1926–1938, Aug. 2009.
[36] D. Dujic, M. Jones, E. Levi, J. Prieto, and F. Barrero, "Switching ripple characteristics of space vector PWM schemes for five-phase two-level voltage source inverters—Part 1: Flux harmonic distortion factors," *IEEE Trans. Ind. Electron.*, vol. 58, no. 7, pp. 2789–2798, Jul. 2011.
[37] S. Tewari, K. Basu, and A. Somani, "Analytical evaluation of the peak-to-peak ripple current in the filter inductor for a space vector modulated grid-tied VSI," in *Proc. Int. Conf. Power Electron., Drives Energy Syst.*, 2014, pp. 1–6.
[38] G. Grandi and J. Loncarski, "Evaluation of current ripple amplitude in three-phase PWM voltage source inverters," in *Proc. Int. Conf.-Workshop Compat. Power Electron.*, 2013, pp. 156–161.
[39] D. Jiang and F. Wang, "Current-ripple prediction for three-phase PWM converters," *IEEE Trans. Ind. Appl.*, vol. 50, no. 1, pp. 531–538, Jan./Feb. 2014.
[40] G. Grandi, J. Loncarski, and O. Dordevic, "Analytical evaluation of output current ripple amplitude in three-phase three-level inverters," *IET Power Electron*., vol. 7, no. 9, pp. 2258–2268, Sep. 2014.
[41] G. Grandi, J. Loncarski, and O. Dordevic, "Analysis and comparison of peak-to-peak current ripple in two-level and multilevel PWM inverters," *IEEE Trans. Ind. Electron.*, vol. 62, no. 5, pp. 2721–2730, May 2015.
[42] L. Chang and T. M. Jahns, "Prediction and evaluation of PWM-induced current ripple in IPM machines incorporating slotting, saturation, and cross-coupling effects," *IEEE Trans. Ind. Appl.*, vol. 54, no. 6, pp. 6015–6026, Nov./Dec. 2018.
[43] Q. Wei, B. Liu, and S. Duan, "Current ripple analysis and controller design for grid-connected converters considering the soft-saturation nature of the powder cores," *IEEE Trans. Power Electron.*, vol. 33, no. 10, pp. 8827–8837, Oct. 2018.
[44] Q. Li, D. Jiang, and Y. Zhang, "Analysis and calculation of current ripple considering inductance saturation and its application to variable switching frequency PWM," *IEEE Trans. Power Electron.*, vol. 34, no. 12, pp. 12262–12273, Dec. 2019.
[45] Magnetics Powder Core Catalog, 2015. [Online]. Available on: www.mag-inc.com.cn.

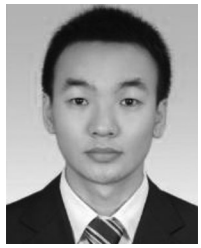

Tao Wang received the B.S. and M.S. degrees in electrical engineering from the HuaZhong University of Science and Technology (HUST), Wuhan, China, in 2015 and 2018, respectively. He is currently working toward the Ph.D. degree at the School of Electrical and Electronics Engineering, HUST.

His research interests include design, control, and modulation of three-phase three-level converters.

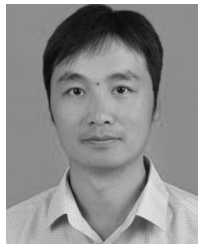

Changsong Chen received the Ph.D. degree in electrical engineering from the Huazhong University of Science and Technology, Wuhan, China, in 2011.

He was a Postdoctoral Research Fellow with the Department of Control Science and Engineering, Huazhong University of Science and Technology, from 2011 to 2013. He is currently a Faculty Member with the School of Electrical and Electronic Engineering, Huazhong University of Science and Technology. His current research interests include renewable energy applications, microgrid, and power electronics applied to electric vehicles.

Tianchang Liu received the B.S. and M.S. degrees in electrical engineering from the HuaZhong University of Science and Technology (HUST), Wuhan, China, in 2017 and 2019, respectively.

She is currently working with State Grid Jiangsu Electric Power Company Research Institute, Nanjing, China. Her research interests include three-phase three-level converters control and application.

Zeyun Chao received the B.S., M.S., and Ph.D. degrees in electrical engineering from the Huazhong University of Science and Technology, Wuhan, China, in 1998, 2001, and 2007, respectively.

Since 1998, she has been a Faculty Member with the College of Electrical and Electronic Engineering, Huazhong University of Science and Technology. Her current research interests include control and applications of power electronic conversion, charging and management of energy storage batteries.

Shanxu Duan (M'14–SM'16) received the B.S., M.S., and Ph.D. degrees in electrical engineering from the Huazhong University of Science and Technology, Wuhan, China, in 1991, 1994, and 1999, respectively.

Since 1991, he has been a Faculty Member with the College of Electrical and Electronic Engineering, Huazhong University of Science and Technology, where he is currently a Professor. His research interests include stabilization, nonlinear control with application to power electronic circuits and systems, fully digitalized control techniques for power electronics apparatus and systems, and optimal control theory and corresponding application techniques for high-frequency pulse width-modulation power converters.

Dr. Duan is a Senior Member of the Chinese Society of Electrical Engineering and a Council Member of the Chinese Power Electronics Society. He was selected as one of the New Century Excellent Talents by the Ministry of Education of China in 2007. He was also the recipient of the honor of "Delta Scholar" in 2009.